Perturbation Estimation Based Nonlinear Adaptive Power Decoupling Control for DFIG Wind Turbine

Kai Shi, Xin Yin, Lin Jiang, *Member, IEEE*, Yang Liu, Yihua Hu, *Senior Member, IEEE*, and Huiqing Wen, *Senior Member, IEEE*

***Abstract*—This paper proposes a perturbation estimation based nonlinear adaptive power decoupling controller for doubly fed induction generator based wind turbines (DFIG-WTs). Perturbation states are defined to include the nonlinearities, uncertainties of the system model, the cross-coupling between control loops, and external disturbances. Perturbation observers are designed to estimate the fast time-varying perturbation states. With perturbation estimation, the DFIG-WT system is fully decoupled, and an output feedback control can be designed for the control of rotor currents. Rotor current references are calculated based on the steady-state relation between active/reactive power and rotor current, and stator dynamic is ignored. The performance of the proposed controller is evaluated and verified via both simulation and experimental tests.**

***Index Terms*—Doubly fed induction generator based wind turbine (DFIG-WT), nonlinear adaptive control, perturbation estimation, power control.**

NOMENCLATURE

v_{ds}, v_{qs}	d-axis and q-axis components of stator voltage, respectively.
v_{dr}, v_{qr}	d-axis and q-axis components of rotor voltage, respectively.
i_{ds}, i_{qs}	d-axis and q-axis components of stator current, respectively.
i_{dr}, i_{qr}	d-axis and q-axis components of rotor current, respectively.

Manuscript received February 13, 2019; accepted April 3, 2019. Date of publication April 16, 2019; date of current version October 18, 2019. This work was supported by the Engineering and Physical Sciences Research Council under Grant EP/J014249/1. Recommended for publication by Associate Editor H. Li. *(Corresponding author: Lin Jiang.)*

K. Shi was with the Department of Electrical Engineering and Electronics, University of Liverpool, Liverpool L69 3GJ, U.K. He is now with the Warwick Manufacturing Group, University of Warwick, Coventry CV4 7AL, U.K. (e-mail:

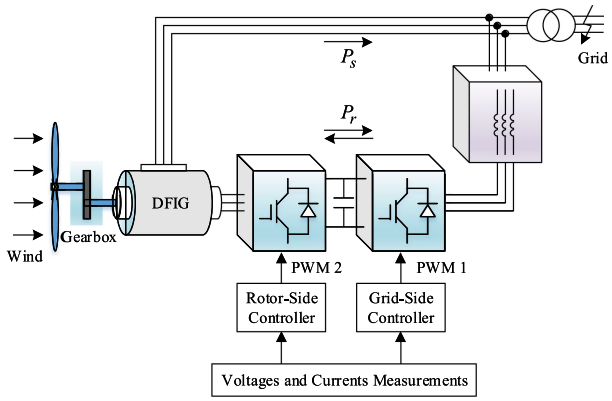

Fig. 1. Grid-connected DFIG-WT with back-to-back converters [1].

[11]; whereas it also shows drawbacks in the following aspects. First, the conventional VC is model-based that makes it sensitive to parameter variations [12]. Moreover, the conventional VC is an asymptotic decoupling control with proportional integral (PI) controllers; its performance may get worse when system operation point changes [13], [14]. Furthermore, conventional VC is realized based on the assumption of a strong external power grid and the neglection of stator resistance, which cannot be satisfied during the transient processes of grid disturbances [15]–[18].

To improve the transient performance of DFIGs, direct power/torque control and advanced nonlinear control strategies have been proposed. The direct power/torque control methods of DFIGs are achieved by directly controlling the scalar variables, which include active/reactive power and torque variables [19]–[22]. Nonlinear control methods, such as sliding-mode control [14], back-stepping control [23], differential flatness based control [24], and feedback linearization control (FLC) [25], etc., have also been applied in the control of DFIGs. The control of DFIGs can be performed using cascade structure that is same as the conventional VC but with improved inner-loop current controllers, such as hysteresis-based controllers [26], [27], FLC [28], [29], and other controllers designed for fault ride-through enhancement [30]–[36]. The FLC theory allows exact linearization and fully decoupling of the nonlinear system such that linear feedback control law can be applied [37]. However, the reliance on full-state feedback and the requirement of the accurate system model make the FLC present poor robustness to parameter uncertainties. Practically, the rotor resistance of the DFIG is varied due to the change of temperature and the use of power electronics converters. The values of inductance are obtained via parameter estimation processes, which risk the control performance by using mismatched parameters in controllers. To remedy the drawbacks of FLC, disturbance observer based FLC (DOFLC) has been proposed in [28], in which a disturbance observer is used to estimate system uncertainties and disturbances. However, the controller in [28] can only handle the unknown constant or slow time-varying disturbance and the disturbance observer used is proposed in [45] with detailed analysis. The previous research suggests that the perturbation estimation based nonlinear control is able to provide real-time compensation of fast time-varying disturbances and has a control structure that is simpler than other nonlinear controllers [39], [40]. Furthermore, the characteristics of those disturbance observer based controllers are reviewed in [38].

This paper proposes a perturbation estimation based nonlinear adaptive power decoupling controller for DFIG-WTs. Different from the controller in [40], which is a four-loop controller, the proposed controller only considers rotor transients and neglects the stator transients. The rotor current references are calculated from the power references based on their steady-state relationship. High-gain perturbation observer is designed to estimate system perturbations, including system cross-couplings, nonlinearities, un-modeled dynamics, and external disturbance. An output feedback controller is designed for the linearized system. Both simulation and experiment studies have been carried out to evaluate the improved performance of proposed controller in comparison with the conventional VC and the controller presented in [28].

II. Perturbation Estimation Based Nonlinear Adaptive Power Decoupling Controller for Grid-Connected DFIG-WT

The proposed controller generates rotor voltage reference values that are required to be injected into rotor windings via PWM converters such that the d- and q-axis rotor currents are able to track their references. The references of rotor currents are calculated based on the active power and reactive power commands at steady state. Hence, the decoupled control of active/reactive powers can be achieved via controlling the corresponding components of rotor currents. As the speed control is usually required by DFIG-WTs in real operation, an outer speed loop is implemented in cascade with the current control loops to calculate the active power reference [41].

The inner current dynamic systems are decoupled and linearized by compensating the perturbations, which are defined to include all system nonlinearities, interactions between the d-axis and the q-axis loop, and external disturbances. A perturbation observer is designed for each subsystem to estimate the system perturbations.

This section presents the model of DFIG-WT at first, followed by the configuration of the control framework with proposed controller. Then, the input–output linearization of the rotor current dynamics is presented. Finally, the design of perturbation observers and the synthesis of control inputs with the proposed controller are presented.

A. Modeling of the DFIG-WT

The dynamic equations of the DFIG stator and rotor currents in the synchronous dq reference frame can be written as [28],

[42] follows:

$$\begin{cases} \dfrac{di_{ds}}{dt} = -\dfrac{R_s}{\sigma L_s} i_{ds} + \left(\omega_s + \dfrac{\omega_r L_m^2}{\sigma L_s L_r}\right) i_{qs} + \dfrac{R_r L_m}{\sigma L_s L_r} i_{dr} \\ \qquad + \dfrac{\omega_r L_m}{\sigma L_s} i_{qr} + \dfrac{1}{\sigma L_s} v_{ds} - \dfrac{L_m}{\sigma L_s L_r} v_{dr} \\ \dfrac{di_{qs}}{dt} = -\left(\omega_s + \dfrac{\omega_r L_m^2}{\sigma L_s L_r}\right) i_{ds} - \dfrac{R_s}{\sigma L_s} i_{qs} - \dfrac{\omega_r L_m}{\sigma L_s} i_{dr} \\ \qquad + \dfrac{R_r L_m}{\sigma L_s L_r} i_{qr} + \dfrac{1}{\sigma L_s} v_{qs} - \dfrac{L_m}{\sigma L_s L_r} v_{qr} \\ \dfrac{di_{dr}}{dt} = \dfrac{R_s L_m}{\sigma L_s L_r} i_{ds} - \dfrac{\omega_r L_m}{\sigma L_r} i_{qs} - \dfrac{R_r}{\sigma L_r} i_{dr} \\ \qquad + \left(\omega_s - \dfrac{\omega_r}{\sigma}\right) i_{qr} - \dfrac{L_m}{\sigma L_s L_r} v_{ds} + \dfrac{1}{\sigma L_r} v_{dr} \\ \dfrac{di_{qr}}{dt} = \dfrac{\omega_r L_m}{\sigma L_r} i_{ds} + \dfrac{R_s L_m}{\sigma L_s L_r} i_{qs} - \left(\omega_s - \dfrac{\omega_r}{\sigma}\right) i_{dr} \\ \qquad - \dfrac{R_r}{\sigma L_r} i_{qr} - \dfrac{L_m}{\sigma L_s L_r} v_{qs} + \dfrac{1}{\sigma L_r} v_{qr}. \end{cases} \tag{1}$$

The stator and rotor flux equations are given as

$$\begin{cases} \phi_{ds} = L_s i_{ds} + L_m i_{dr} \\ \phi_{qs} = L_s i_{qs} + L_m i_{qr} \\ \phi_{dr} = L_m i_{ds} + L_r i_{dr} \\ \phi_{qr} = L_m i_{qs} + L_r i_{qr}. \end{cases} \tag{2}$$

The electromagnetic torque can be expressed with stator fluxes and currents as

$$T_{em} = \frac{3p}{2} \left(\phi_{ds} i_{qs} - \phi_{qs} i_{ds}\right). \tag{3}$$

The stator active and reactive powers can be expressed as

$$\begin{cases} P_s = 1.5 \left(v_{ds} i_{ds} + v_{qs} i_{qs}\right) \\ Q_s = 1.5 \left(v_{qs} i_{ds} - v_{ds} i_{qs}\right). \end{cases} \tag{4}$$

The mechanical equation that describes rotor speed dynamics is expressed as

$$J \frac{d\omega_{\mathrm{mec}}}{dt} = T_{em} - B\omega_{\mathrm{mec}} - T_{\mathrm{mec}}. \tag{5}$$

The relationship between ω_{mec} and ω_r is $\omega_r = \text{pole pairs} \times \omega_{\mathrm{mec}}$.

The wind power model can be expressed according to the mechanical power captured from the wind, which is described as [43] follows:

$$P_w = \frac{1}{2} \rho A C_p \left(\lambda, \beta\right) v_w^3. \tag{6}$$

To maximize the mechanical power extracted by the wind turbine, the rotor speed reference of DFIG-WT is given based on power–speed curve as

$$\omega_{\mathrm{mec}}^* = \lambda_{\mathrm{opt}} v_w / D \tag{7}$$

where λ_{opt} is the optimal tip-speed ratio that results in the maximum value of $C_p(\lambda, \beta)$ and D is the blade length of the wind turbine.

B. Active/Reactive Power Decoupling Control

The proposed controller works with the control framework shown in Fig. 2. The SVO dq frame is used by aligning the q-axis with the stator voltage vector. The proposed controller requires measurements of d- and q-axis rotor currents and the rotor current references are calculated from the stator active and reactive power references, respectively. The rotor speed command can be obtained based on the optimal power–speed curve, and the reactive power reference is set based on power factor requirement. Finally, the required rotor voltages can be applied to rotor winding via RSC using sinusoidal PWM (SPWM) techniques.

For a given active and reactive power references, the d- and q-axis rotor current references can be calculated based on the steady-state relationship between active/reactive power and rotor current as [30]

$$i_{dr}^* = \frac{2}{3} \frac{L_s}{L_m} \frac{Q_s^*}{v_{qs}} - \frac{v_{qs}}{\omega_s L_m}, i_{qr}^* = \frac{2}{3} \frac{L_s}{L_m} \frac{P_s^*}{v_{qs}}. \tag{8}$$

It is noted that the measurement of v_{qs} in (8) can be replaced by its nominal value, which reduces one measurement input. The active power reference is obtained from the outer speed loop, which converts the speed error into active power reference using PI controller as [44]

$$P_s^* = k_p \left(\omega_r - \omega_r^*\right) + k_i \int \left(\omega_r - \omega_r^*\right) dt. \tag{9}$$

C. Input–Output Linearization

The rotor current dynamics in (1) can be rewritten as

$$\begin{cases} \dot{i}_{dr} = f_d + g_d v_{dr} \\ \dot{i}_{qr} = f_q + g_q v_{qr} \end{cases} \tag{10}$$

where

$$\begin{cases} f_d = \dfrac{R_s L_m}{\sigma L_s L_r} i_{ds} - \dfrac{\omega_r L_m}{\sigma L_r} i_{qs} - \dfrac{R_r}{\sigma L_r} i_{dr} \\ \qquad + \left(\omega_s - \dfrac{\omega_r}{\sigma}\right) i_{qr} - \dfrac{L_m}{\sigma L_s L_r} v_{ds} \\ f_q = \dfrac{\omega_r L_m}{\sigma L_r} i_{ds} + \dfrac{R_s L_m}{\sigma L_s L_r} i_{qs} - \left(\omega_s - \dfrac{\omega_r}{\sigma}\right) i_{dr} \\ \qquad - \dfrac{R_r}{\sigma L_r} i_{qr} - \dfrac{L_m}{\sigma L_s L_r} v_{qs} \\ g_d = g_q = \dfrac{1}{\sigma L_r}. \end{cases} \tag{11}$$

The rotor current dynamics in (10) can be decoupled and linearized by choosing the control inputs as

$$\begin{cases} v_{dr} = \frac{1}{g_d} \left(u_d - f_d\right) \\ v_{qr} = \frac{1}{g_q} \left(u_q - f_q\right). \end{cases} \tag{12}$$

which linearizes the system and yields

$$\begin{cases} \dot{i}_{dr} = u_d \\ \dot{i}_{qr} = u_q. \end{cases} \tag{13}$$

The feedback control law can be designed for the linear system (13) to achieve the tracking control of i_{dr} and i_{qr} with references

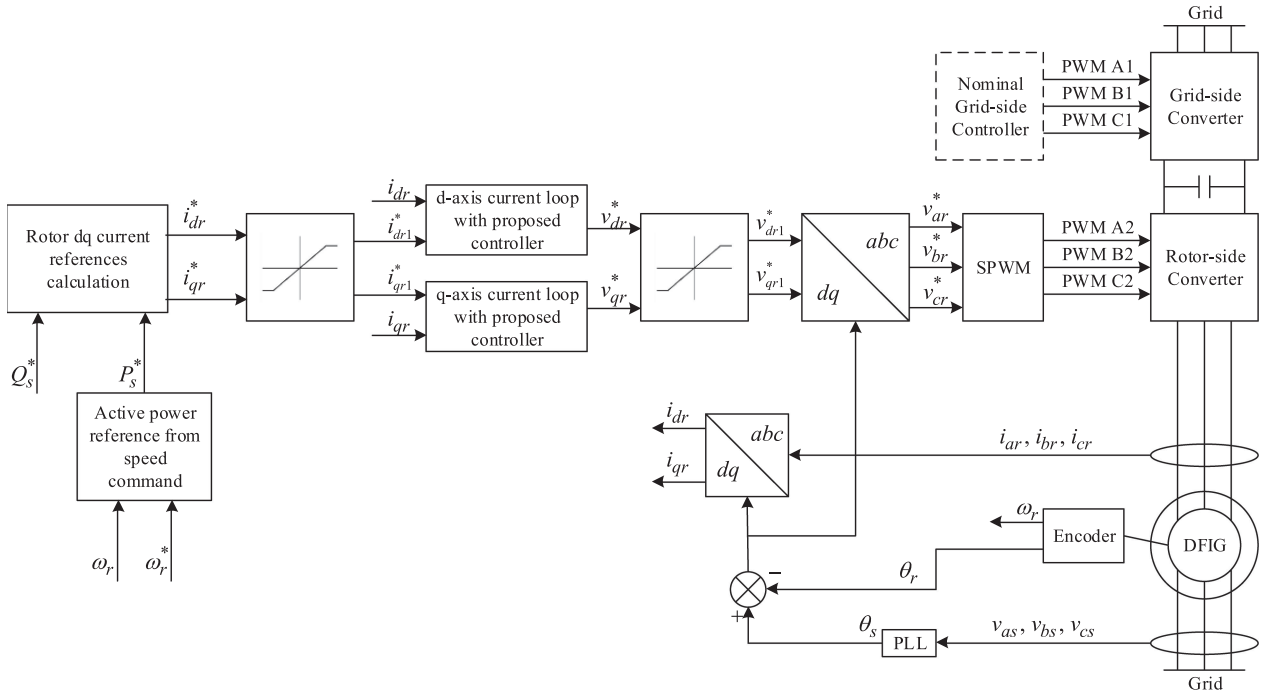

Fig. 2. Control scheme of grid-connected DFIG-WT using proposed controller.

i_{dr}^* and ${i_{qr}}^*$ as

$$\begin{cases} u_d = \dot{i}_{dr}^* - k_d \left(i_{dr} - i_{dr}^*\right) \\ u_q = \dot{i}_{qr}^* - k_q \left(i_{qr} - i_{qr}^*\right). \end{cases} \tag{14}$$

By substituting (13) into (14), the dynamics of tracking errors $e_d = i_{dr} - i_{dr}^*, e_q = i_{qr} - i_{qr}^*$ can be obtained as

$$\begin{cases} \dot{e}_d + k_d e_d = 0 \\ \dot{e}_q + k_q e_q = 0. \end{cases} \tag{15}$$

The poles of (15) are placed in the left-half complex plane by choosing positive values for k_d and k_q such that the error dynamics are exponentially stable.

D. Proposed Nonlinear Adaptive Controller (NAC)

Perturbation states are defined to include system nonlinearities, cross-couplings between subsystems, parameter uncertainties, and external disturbances. According to (10) and (11), the system perturbation can be expressed as

$$\begin{cases} \Psi_d = f_d + \left(g_d - g_{d0}\right) v_{dr} \\ \Psi_q = f_q + \left(g_q - g_{q0}\right) v_{qr} \end{cases} \tag{16}$$

where g_{d0} and g_{q0} are the nominal values of g_d and g_q, respectively. Then, (10) can be rewritten as

$$\begin{cases} \dot{i}_{dr} = \Psi_d + g_{d0} v_{dr} \\ \dot{i}_{qr} = \Psi_q + g_{q0} v_{qr}. \end{cases} \tag{17}$$

The perturbations are treated as the extended-order states, so that new state variables can be defined as $x_{d1} = i_{dr}, x_{d2} = \Psi_d$, $x_{q1} = i_{qr}$, and $x_{q2} = \Psi_q$. By choosing the outputs as $y_d = x_{d1}$ and $y_q = x_{q1}$, (17) can be expressed by two subsystems as

$$\begin{cases} \dot{x}_{d1} = x_{d2} + g_{d0} v_{dr} \\ \dot{x}_{d2} = \dot{\Psi}_d \left(\bullet\right) \\ y_d = x_{d1} \end{cases} \tag{18}$$

$$\begin{cases} \dot{x}_{q1} = x_{q2} + g_{q0} v_{qr} \\ \dot{x}_{q2} = \dot{\Psi}_q \left(\bullet\right) \\ y_q = x_{q1}. \end{cases} \tag{19}$$

Assuming perturbation terms Ψ_d and Ψ_q are unknown, the perturbation observer needs to be designed for subsystem (18) and (19) to obtain the estimation of the perturbation states. Here, the linear observer is used in the design of perturbation observers [39]. The perturbation observers for subsystem (18) and (19) are designed as

$$\begin{cases} \dot{\hat{x}}_{d1} = \hat{x}_{d2} + h_{d1} \left(x_{d1} - \hat{x}_{d1}\right) + g_{d0} v_{dr} \\ \dot{\hat{x}}_{d2} = h_{d2} \left(x_{d1} - \hat{x}_{d1}\right) \end{cases} \tag{20}$$

$$\begin{cases} \dot{\hat{x}}_{q1} = \hat{x}_{q2} + h_{q1} \left(x_{q1} - \hat{x}_{q1}\right) + g_{q0} v_{qr} \\ \dot{\hat{x}}_{q2} = h_{q2} \left(x_{q1} - \hat{x}_{q1}\right) \end{cases} \tag{21}$$

where h_{d1} and h_{d2} are observer gains of perturbation observer (20) for subsystem (18), h_{q1} and h_{q2} are observer gains of perturbation observer (21) for subsystem (19), and the embellishment "$\hat{}$" stands for the estimated value of a variable. The pole placement technique is applied for selecting the observer gains such that the observer error dynamics of each subsystem are Hurwitz. The observer gains h_{d1} and h_{d2} are selected such that the roots of being in the open left-half plane. Similarly, the observer gains h_{q1} and h_{q2} are chosen to place the poles of $s^2 + h_{q1} s + h_{q2} = 0$ in the open left-half plane.

It should point out that the main contribution of this paper against [28] is that the proposed perturbation observer can estimate unknown fast time-varying unknown dynamics, whereas the observer in [28] can only estimate unknown constant or slow time-varying disturbance based on the assumption of zero change rate of the disturbances. Note that both observers are exponentially convergent with rates by setting correspondent observer gains, but the observer [28] is only valid under the assumption of zero change rate of the disturbances. However, as the converging rate of the observer is usually set to be 5–10 times faster than the dynamic of estimated disturbance, the converging rate of the proposed observer will be set much faster than the one in [28], with the cost of a relatively larger observer gains.

Finally, the control inputs can be synthesized based on the linear feedback law (14) and the perturbation observer (20) and (21) as

$$\begin{cases} v_{dr} = \frac{1}{g_{d0}}\left[\dot{i}^*_{dr} - k_d\left(i_{dr} - i^*_{dr}\right) - \widehat{\Psi}_d\right] \\ v_{qr} = \frac{1}{g_{q0}}\left[\dot{i}^*_{qr} - k_q\left(i_{qr} - i^*_{qr}\right) - \widehat{\Psi}_q\right]. \end{cases} \tag{22}$$

As the separation principle of separately designing observer and controller is no longer valid for a nonlinear system, the stability of the overall closed-loop system should be investigated considering all subsystems together, including perturbation observer (20), (21), nonlinear control (22), and the controlled system (1) and (10). The stability analysis of overall closed-loop system is given in Appendix B.

The block diagram of the proposed controller is shown in Fig. 3. The implementation of the proposed controller only requires the information of rotor current states and the nominal value of g_{d0} and g_{q0}. Although the values of the stator currents are not involved in the proposed control loops, the measurement of the stator currents is still needed in the overall control system for DFIG-WT. It implies a simpler structure and less dependence on model information than the FLC. With proper observer gains selected using pole placement techniques, the perturbation observers can actively estimate and compensate perturbations. It is worthy to note that there is a tradeoff on observer gain selection between the convergence speed and sensitivity to measurement noise since the increase of observer gains can amplify the measurement noise. Another contribution of the proposed controller is that the proposed observer (20)–(21) does not rely on the DFIG parameters, which reduces the complexity of the controller and improves the robustness to measurement noise and parameter uncertainties as well. This is another contribution of the proposed method comparing to [28].

E. Current and Voltage Saturation Strategies for RSC

To consider the voltage and current saturation of the RSC, upper bounds of the voltage and current references need to be set. The priority of the current reference is given to the active power control, hence the control of is prioritized [46]. Given, $I_{\max}$ as the upper bound of the current magnitude, the q-axis

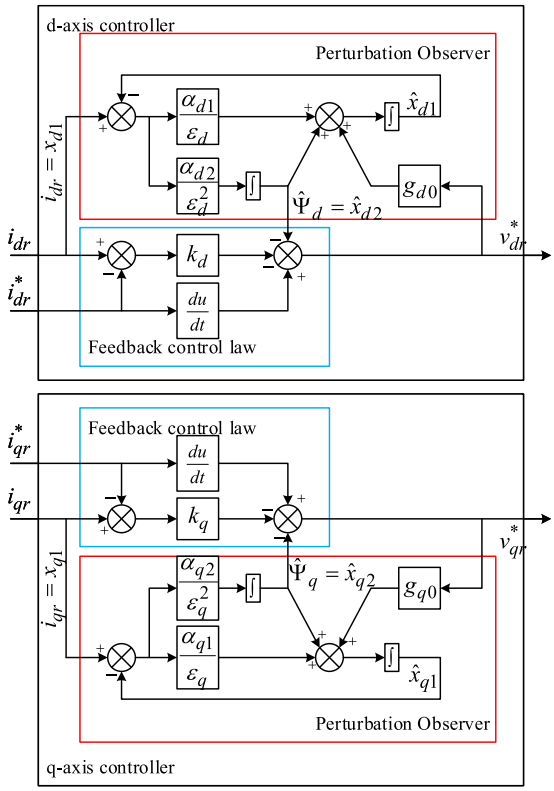

Fig. 3. Control block diagram of proposed controller without saturation of RSC.

current reference after saturation is given as

$$i^*_{qr1} = \begin{cases} \operatorname{sign}(i^*_{qr}) \bullet I_{\max}, & \left|i^*_{qr}\right| \geq I_{\max} \\ i^*_{qr}, & \left|i^*_{qr}\right| < I_{\max} \end{cases} \tag{23}$$

and the d-axis current reference after saturation is

$$i^*_{dr1} = \begin{cases} \operatorname{sign}(i^*_{dr}) \bullet \sqrt{I^2_{\max} - i^{*2}_{qr}}, & \left|i^*_{dr}\right| \geq \sqrt{I^2_{\max} - i^{*2}_{qr}} \\ i^*_{dr}, & \left|i^*_{dr}\right| < \sqrt{I^2_{\max} - i^{*2}_{qr}}. \end{cases} \tag{24}$$

The value of $I_{\max}$ is set to be the rated value of the rotor current amplitude [5].

With respect to the saturation of the rotor voltage, a general approach in [44] is used, in which the magnitude of the rotor voltage reference, namely $V^*_r = \sqrt{v^{*2}_{dr} + v^{*2}_{qr}}$, is limited by setting an upper bound $V_{\max}$, which yields

$$V^*_{r1} = \begin{cases} V_{\max}, & V^*_r \geq V_{\max} \\ V^*_r, & V^*_r < V_{\max} \end{cases} \tag{25}$$

whereas the angle between v^*_{dr} and v^*_{qr}, namely $\theta^*_r = \arctan(v^*_{qr}/v^*_{dr})$, is unchanged. Therefore, the rotor voltage references processed by the saturation approach can be obtained by

$$\begin{cases} v^*_{dr1} = V^*_{r1} \bullet \cos\theta^*_r \\ v^*_{qr1} = V^*_{r1} \bullet \sin\theta^*_r. \end{cases} \tag{26}$$

TABLE I
PARAMETERS OF THE SIMULATED DFIG-WT

Parameters	Quantity
Nominal power	1.5/0.9 MVA
Nominal voltage	575 Vrms 60 Hz
Pole pairs	3
Stator/rotor turns ratio	1:3
Stator resistance	0.0026 Ω (0.023 pu)
Rotor resistance	0.0029 Ω (0.016 pu)
Stator leakage inductance	0.077 mH (0.18 pu)
Rotor leakage inductance	0.083 mH (0.16 pu)
Mutual inductance	2.5 mH (2.9 pu)
Inertia constant	0.685 s
Wind speed	12 m/s
Initial rotor speed	1.2 pu
Transmission Line length	10 km
No. of wind turbines	1

With SPWM-based VSC control strategy, the amplitude of the maximum achievable fundamental output voltage of VSC without over-modulation is $V_{\rm dc}/2$. As the limit of the dc-link voltage is typically 1.2 times of its nominal value $V_{\rm dc\_nom}$, so $V_{\max}$ can be set to be $V_{\max} = 1.2V_{\rm dc\_nom}/2$.

III. Simulation Studies

The performance of the proposed NAC has been tested via simulation in MATLAB/Simulink. The simulated system is based on the demo with the detailed model of a DFIG-WT and power converters provided by the SimPowerSystems library. The system parameters are given in Table I. Comparison studies have been undertaken among the conventional VC, DOFLC proposed in [28], and proposed NAC. The DOFLC has been briefly recalled in Appendix A. The controllers designed in the continuous-time domain have been discretized using forward Euler's method for digital control implementation. The PWM frequency is set as 5 kHz with SPWM technique.

When implementing the perturbation observer in simulation, the observer gains are selected as $h_{d1} = h_{q1} = 2 \times 10^4$ and $h_{d2} = h_{q2} = 1 \times 10^8$ so all poles of the observer error dynamics are placed at $\gamma = 10\,000$. The values of g_{d0} and g_{q0} are constants obtained based on the system parameters.

A. Decoupled Control of Active/Reactive Power Under Step References

The decoupled control of the active and reactive power of the DFIG is tested by evaluating the step responses of the active and the reactive power. The step functions of references are filtered by a transfer function such that the fast change of reference values can be avoided. The simulation results are shown in Fig. 4, which indicates that the DOFLC and the NAC provide the faster speed of response than the VC does. The NAC has the same step change performance as the DOFLC. Without uncertainty and all external disturbance is correctly measured, the DOFLC provide the same performance as FLC as the disturbance observer in DOFLC does not make an effort to estimate the uncertainty. So, the simulation result suggests that the proposed NAC is able to provide the dynamic performance as good as the FLC does.

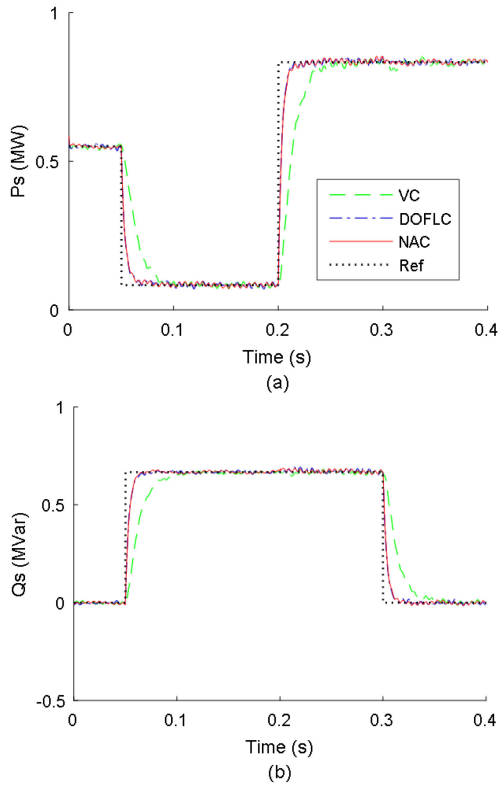

Fig. 4. Step responses of the stator power. (a) Active power. (b) Reactive power.

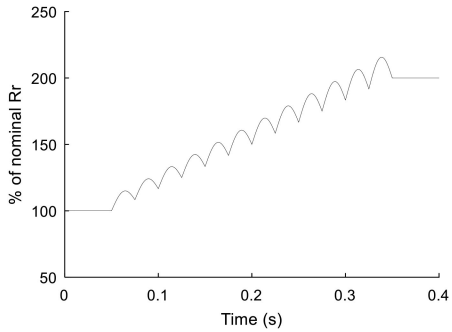

Fig. 5. Variation of actual rotor resistance value applied to the system in simulation.

B. Decoupled Control of Active/Reactive Power Under Sinusoidal References and Uncertainties

The DFIG may be required to generate sinusoidal active/reactive power in case of the demand for system damping [28]. The performance of sinusoidal reference tracking has been tested. Moreover, uncertainties including a time-varying unknown rotor resistance and a 20% mismatched error of L_m in the controllers have been introduced. Fig. 5 shows the time-varying rotor resistance applied in the simulation. The tracking performance of the sinusoidal reference is shown in Fig. 6. There is a 20 Hz sinusoidal signal with 0.6 MW amplitude added to the active power reference at $t = 0.1$ s and then a 20 Hz sinusoidal signal with 0.6 Mvar amplitude is added to the reactive power reference at $t = 0.2$ s. The tracking performance provided by

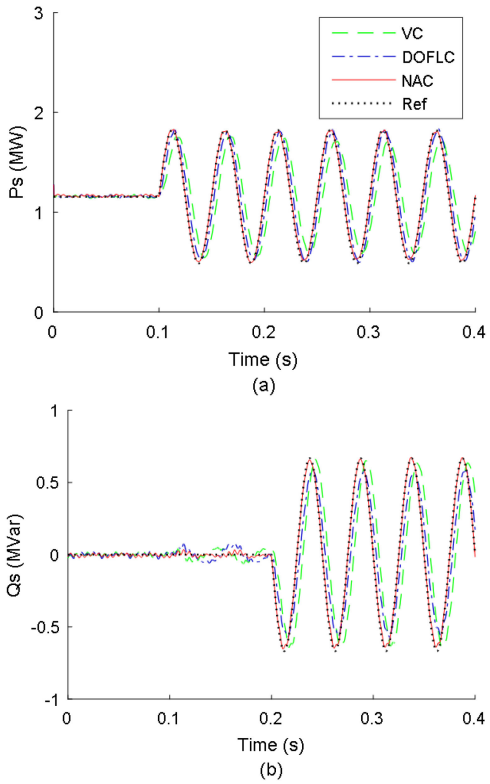

Fig. 6. Power reference tracking with uncertainties. (a) Active power. (b) Reactive power.

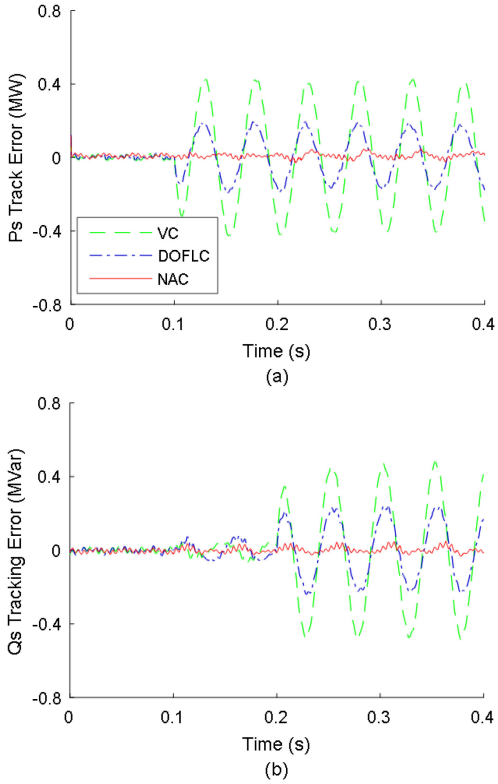

Fig. 7. Tracking errors with uncertainties. (a) Active power. (b) Reactive power.

the VC has an obvious lag between the power references and the real active/reactive power. The tracking errors are shown in Fig. 7, in which the NAC is with the maximum tracking error of 0.1 MW and 0.05 Mvar, the VC is with maximum tracking errors of 0.43 MW and 0.48 Mvar, whereas the DOFLC is with 0.2 MW and 0.24 Mvar maximum tracking errors. The fast time-varying uncertainties in the tracking control caused by the time-varying rotor resistance and the mismatched value of inductance can be actively estimated and compensated by the estimated perturbations using the perturbation observer of the NAC. The tracking performance with fast time-varying uncertainty is improved when using the proposed NAC.

C. Low-Voltage Ride-Through (LVRT) Capabilities With Uncertainty

The voltage dip happened at the stator terminal will cause large inrush current that may damage the power electronic devices and trip the wind energy system. The LVRT capabilities of the DFIG with three controllers have been evaluated via examining the rotor current response to the voltage dip. The 20% mismatched error of the value of L_{m} is applied in controllers during simulation. It is shown in Fig. 8(a) that a 20% dip of grid voltage is applied at $t = 0.05$–0.15 s, whereas the DFIG-WT is operating at steady state with 1.2 p.u. rotor speed. Fig. 8(b) shows the rotor current magnitude in response to this voltage dip. The peak transient current of the DFIG with the VC is 1.05 kA, whereas the peak rotor current with DOFLC

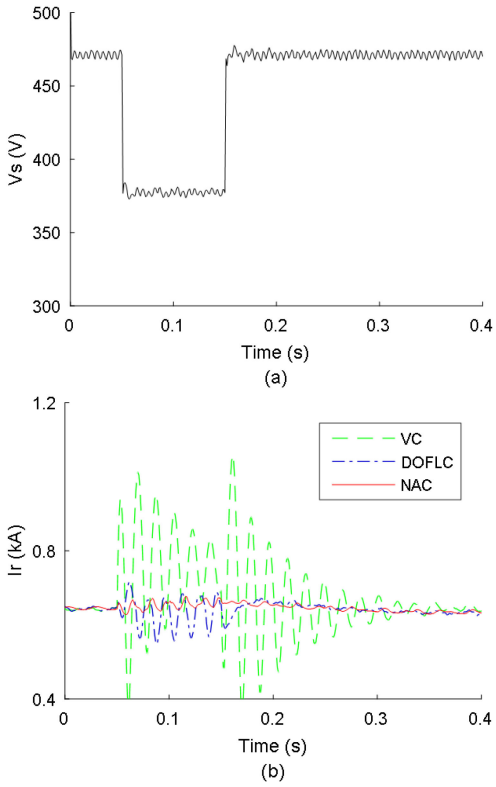

Fig. 8. Responses of rotor current magnitude to the 20% dip of stator terminal voltages with uncertainty. (a) Stator voltage magnitude. (b) Rotor current magnitude.

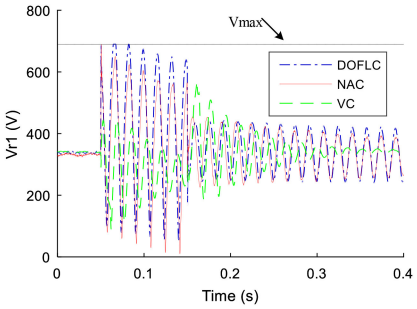

Fig. 9. Amplitude of the calculated rotor voltage after saturation during and after a voltage dip.

and NAC is 0.72 and 0.68 kA, respectively. With NAC, the peak rotor current during and after the voltage dip is reduced by 35% compared to VC and 5% comparing to DOFLC. The NAC also reduces the oscillations of the rotor current amplitude and recover to its pre-fault value fast after the restoration of the grid voltage. With mismatched mutual inductance, the disturbance and perturbation observers need to estimate fast time-varying disturbances during the voltage dip due to the oscillating of the natural flux. Therefore, the advantage of estimating fast time-varying with proposed perturbation observers is revealed.

The RSC controller will increase the rotor voltage to compensate the disturbance caused by the voltage dip at the stator and so as to constrain the converter current. To demonstrate the effect of the saturation of RSC, the rotor voltage amplitude from three controllers are shown in Fig. 9, in which rotor voltage from all cases has been limited below the $V_{\max}$. Note that 20% voltage dip is used in this case, it can predict that under a case with a bigger voltage dip level, the amplitude of the rotor voltage will increase and approach more closely to the $V_{\max}$.

The rotor current is decided by both the injected rotor voltage via RSC and the induced electromotive force (EMF) [47]. During the transient period under the voltage dip, the induced EMF is consequently large. To compensate the induced EMF, a large output voltage of RSC is expected to reduce the rotor current. The result shows that both the DOFLC and the proposed NAC require larger output voltage of the RSC to constrain the transient rotor current when comparing to the VC and the NAC requires a smaller rotor voltage than the DOFLC and results in a smaller rotor current. Note that for both NAC and DOFLC, the induced EMF component is same under the same voltage dip level. However, the DOFLC cannot accurately estimate the disturbance under the voltage dip in the presence of the mismatched parameter L_{m} as the disturbance changes quickly, which results in the induced transient components that cannot be completely compensated. As both NAC and DOFLC use the same linear controller, the inaccurate compensation with DOFLC causes a larger peak rotor current and longer oscillation period, whereas the NAC can accurately estimate the disturbance, hence a smaller peak value and shorter oscillation period.

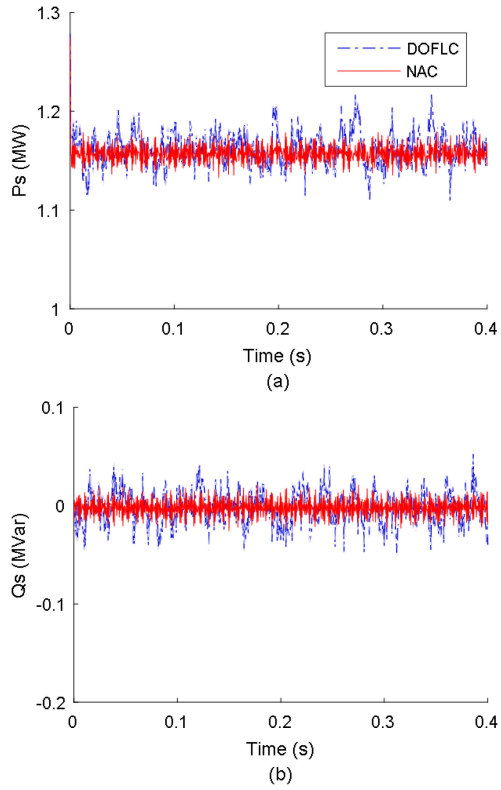

Fig. 10. Steady-state performance of DFIG with measurement noise. (a) Stator active power. (b) Stator reactive power.

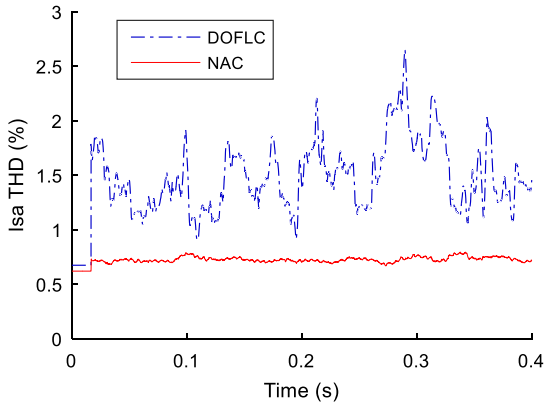

Fig. 11. THD of phase A stator current with measurement noise.

D. Robustness Against Measurement Noise

Sensor noise is inevitable and will degrade the control performance by distorting the controlled system inputs. To test the controller performance with measurement noise, a Gaussian noise with 0 mean and variance 2% of the signals' true rms values is applied. The maximum value of the noise is limited to 5% of the true root mean square (rms) values. The active/reactive power performance and stator current THD in steady state are studied in Figs. 10 and 11, respectively. The DFIG with DOFLC has more serious distortion in both active and reactive power, whereas the influence of noise in NAC is smaller with NAC. With respect to the THD performance shown in Fig. 10, the DOFLC results in a higher stator current THD (peak value is

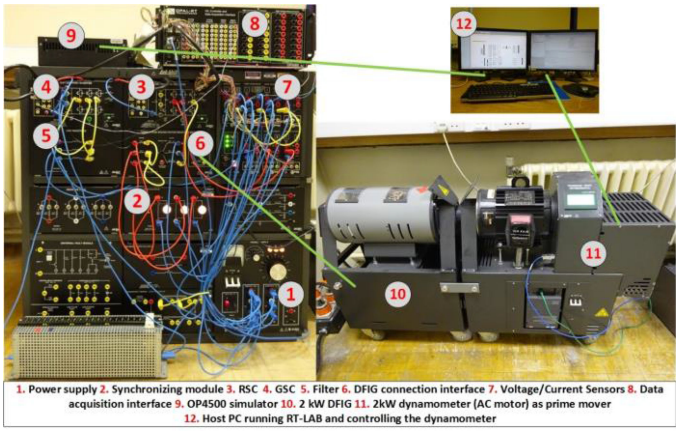

Fig. 12. Experimental setup with a LabVolt 2-kW DFIG kit and OP4500 simulator.

TABLE II
PARAMETERS OF LABVOLT 2-KW DFIG SYSTEM

Parameters	Quantity
Rated power	2 kW
Stator voltage	110 Vrms 50 Hz
Pole pairs	2
Stator/rotor turns ratio	0.3
Stator resistance	2.3 Ω
Rotor resistance	2.5 Ω
Stator leakage inductance	0.02 H
Rotor leakage inductance	0.02 H
Mutual inductance	0.35 H
Inertia constant	0.107 kg.m^2
Filter inductance	0.06 H
DC voltage	400 V
PWM frequency	5000 Hz

2.7%) than NAC (peak value is 0.7%). Although the observers magnify the noise and cause distortion in controlled variables, which is the drawback of both DOFLC and NAC, the proposed NAC does not need full state feedbacks so the noise of stator voltages and currents can be isolated with NAC.

IV. EXPERIMENTAL VALIDATION

Fig. 12 shows the experimental setup of the DFIG system with back-to-back insulated gate bipolar transistor (IGBT) converters. A 2-kW DFIG (LabVolt 8505-A0) is driven by an ac motor (LabVolt 8540), the rotor windings of DFIG are connected to two back-to-back IGBT converters (LabVolt 8857-10), and the stator windings are supplied by a 110 V 50 Hz three-phase voltage via a Variac that is connected to a 240 V 50 Hz three-phase socket. The controllers are implemented using OP4500 simulator with analog signals from the voltage/current measurement units, and digital signals from an encoder fed in. The converters are driven by duty-cycle controlled PWM signals, which are generated by OP4500 simulator. The experiment system parameters are listed in Table II.

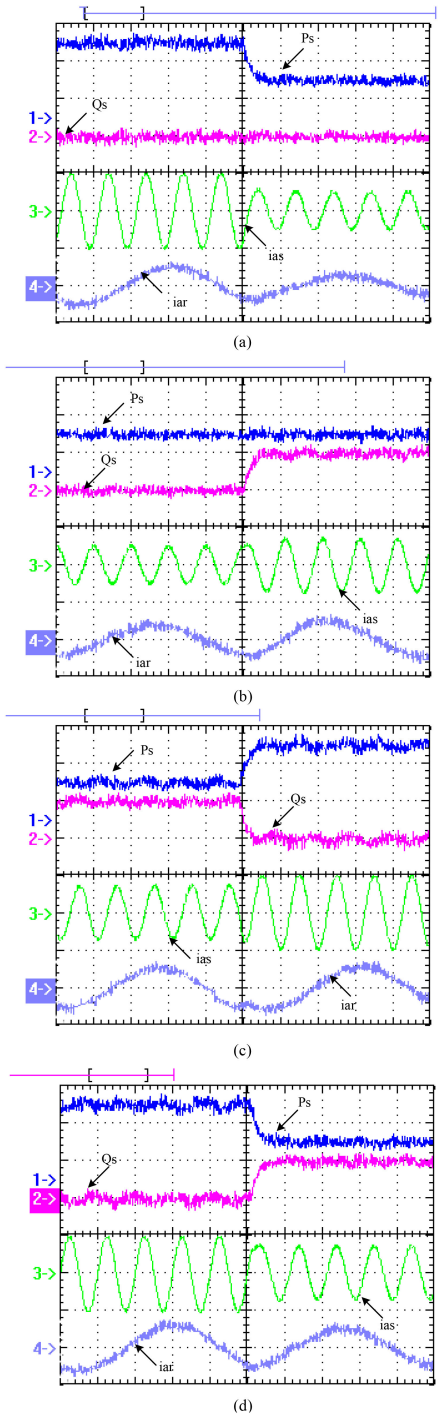

Fig. 13. DFIG active/reactive power step response with NAC. (a) Step down of P_s. (b) Step up of Q_s. (c) Step up of P_s and step down of Q_s. (d) Step down of P_s and step up of Q_s (divisions: P_s – 500 W/div, Q_s – 500 var/div, ias – 6 A/div, iar – 2 A/div, time – 20 ms/div).

A. Decoupled Control of Active and Reactive Power Outputs

The decoupled active/reactive power control with the proposed controller is tested at 1800 r/min (1.2 p.u.) rotor speed, which is shown in Fig. 13. The step changes between 1 and 0.5 kW are applied to active power, and step changes between 0 and 500 var are applied to reactive power. Fig. 13(a) shows

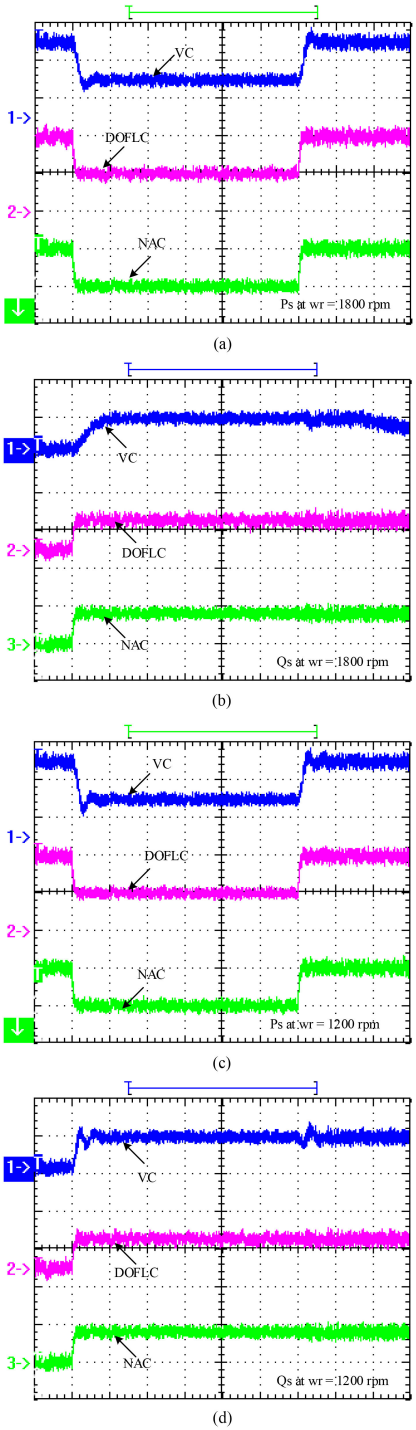

Fig. 14. DFIG active/reactive power step response at different rotor speeds. (a) P_s at $\omega_r = 1800$ r/min. (b) Q_s at $\omega_r = 1800$ r/min. (c) P_s at $\omega_r = 1200$ r/min. (d) Q_s at $\omega_r = 1200$ r/min (divisions: P_s – 500 W/div, Q_s – 500 var/div, time –100 ms/div).

the decrease of active power while reactive power keeps constant, whereas Fig. 13(b) shows the step up of reactive power while active power is constant. Fig. 13(c) and (d) present the simultaneous change of active and reactive power. The control of active/reactive power with NAC can be fully decoupled, and the step response is fast (within 20 ms) without overshoots and oscillations.

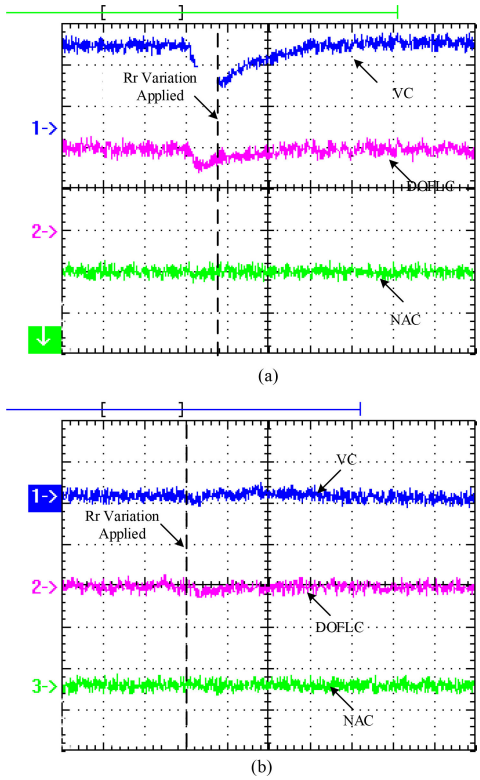

Fig. 15. DFIG active/reactive power response with uncertainty. (a) Active power. (b) Reactive power (divisions: P_s – 500 W/div, Q_s – 500 var/div).

B. Operation at Different Operating Points

Further tests of the active/reactive power control at different rotor speed have been done, and the experiment results are shown in Fig. 14. It can be observed that the step response of VC is slower than DOFLC NAC and has small overshoots in Fig. 14 (a) and (b) when the DFIG operates at the super-synchronous speed. In comparison, Fig. 14(c) and (d) show the step response at sub-synchronous rotating speed. The larger overshoot and more oscillations can be observed with VC when comparing to the VC responses at super-synchronous. The varying of operation points can cause the performance degradation when using VC, whereas it does not impact the performance of DOFLC and NAC.

C. Robustness Against Parameter Uncertainties

In order to emulate the parameter variations, variable resistors are connected in series between converter and rotor windings. A sudden change of the variable resistors from 0 to 5 Ω is applied when the DFIG is operating at steady state and a 20% mismatched error of the value of L_m is applied. The experiment results are shown in Fig. 15(a) and (b). Fig. 15(a) shows that the DFIG controlled by VC has a 400 W drop of active power, which is recovered to the set point in 40 ms. With DOFLC, the influence of the fast change of rotor resistance is reduced and a 150 W drop of the active power is observed. With proposed NAC, there is no significant influence of rotor resistance variation shown on the active/reactive

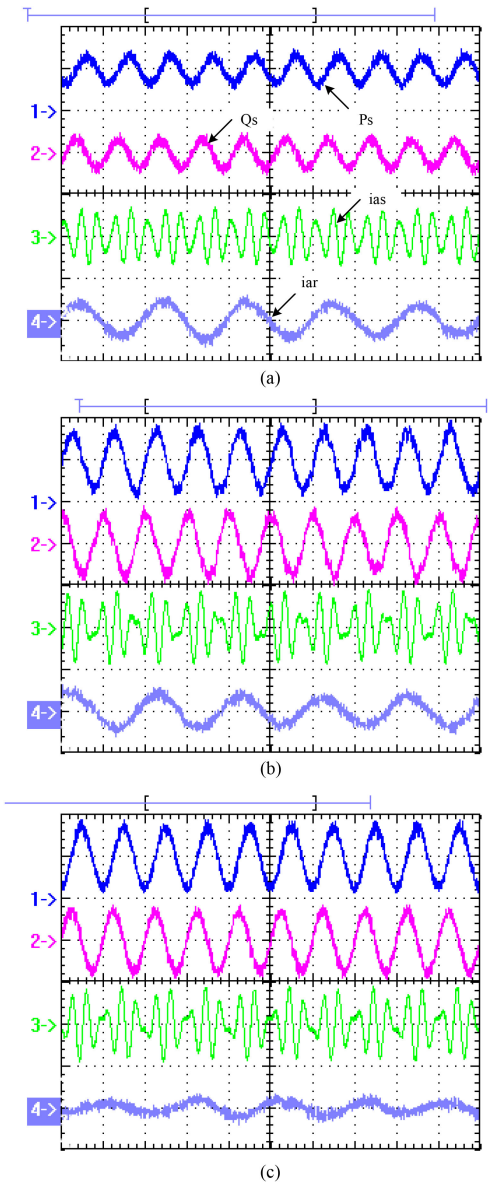

Fig. 16. DFIG active/reactive power tracking control responses with sinusoidal references applied and uncertainty. (a) VC. (b) DOFLC. (c) NAC (divisions: P_s – 500 W/div, Q_s – 500 var/div, time – 50 ms/div).

power due to the ability of NAC in estimating fast-varying uncertainties.

D. Sinusoidal Power Reference Tracking With Parameter Uncertainties

The sinusoidal power reference tracking control has been tested, and the experiment results are shown in Fig. 16. A 20-Hz sinusoidal active and reactive power references are applied in addition to constant power references, which are 500 W for active power reference and 0 var for reactive power reference. The amplitudes of the sinusoidal active and reactive power references are 300 W and 300 var, respectively. A 20% mismatched error of the value of L_m is applied. When the active power and the reactive power are controlled to track sinusoidal references, the stator and rotor currents are neither balanced under the

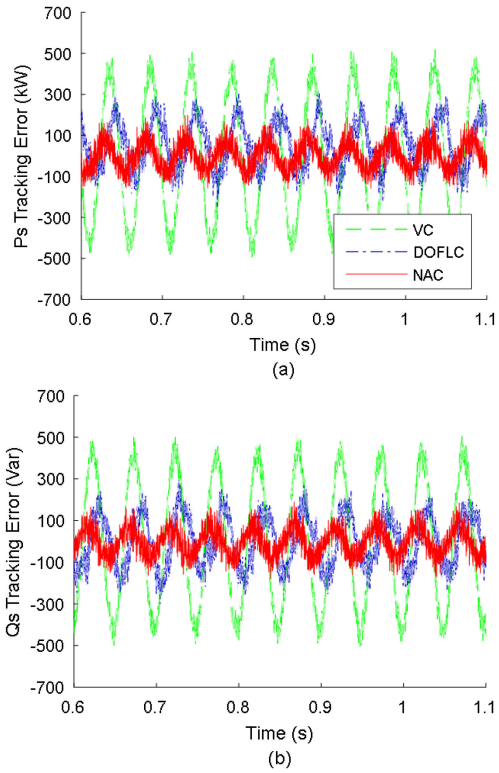

Fig. 17. Tracking errors with sinusoidal reference with uncertainties. (a) Active power. (b) Reactive power.

balanced grid conditions nor in sinusoidal shapes. The comparison results of the tracking control performance are presented in Fig. 17. With VC, the maximum tracking errors of the active and the reactive power are around 500 W and 500 var, respectively. The DFIG controlled by the DOFLC or the NAC results in relatively smaller tracking errors, whose maximum values are less than 300 W for active power and 300 var for reactive power. Comparing Fig. 17 with the simulation results in Fig. 7, increased tracking errors with NAC in Fig. 17 can be seen easily due to the higher control time-delay and the smaller observer gains in experimental tests than simulation studies. However, Fig. 17 still suggests the smaller tracking error with NAC than with DOFLC, which draws the same conclusion as the simulation studies.

E. LVRT Capability Considering Parameter Uncertainties

A 20% dip (30 V) of the stator voltage is applied via turning the Variac with a 20% mismatched error of L_m to test the DFIG responses to voltage dips. The responses of DFIG controlled by VC, DOFLC, and NAC are shown in Fig. 18. It can be observed in Fig. 18(a) that there are oscillations of active/reactive power with VC and the increase of stator current when the voltage dip is applied. The small increase and distortion can also be observed in the rotor current of the DFIG controlled by VC at the same time. In comparison, no significant oscillation of power or inrush current can be observed in Figs. 18(b) and 18(c) with DOFLC or NAC. The THD values of the stator current with those controllers are shown in Fig. 18(d), which presents in detail the

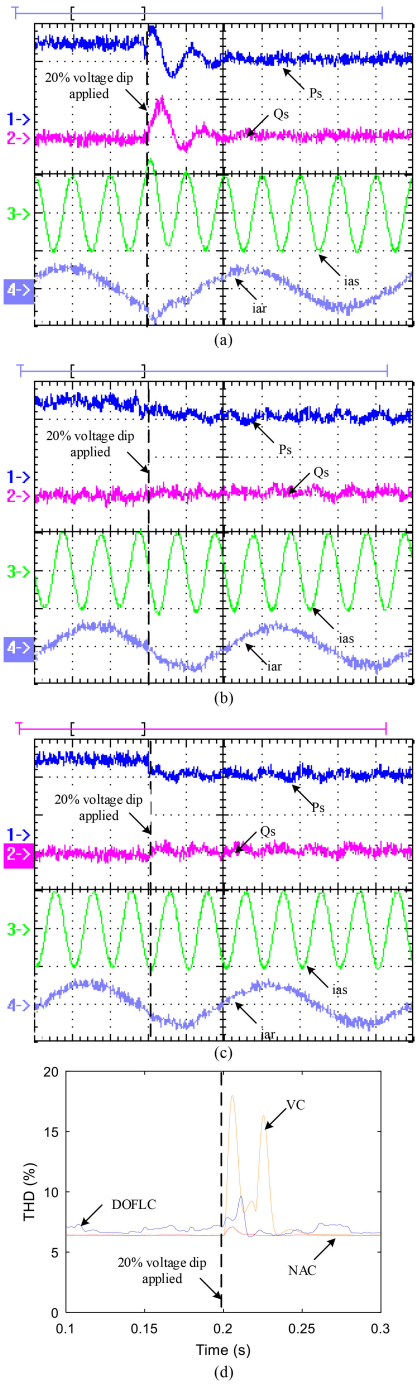

Fig. 18. LVRT capability test with uncertainty. (a) VC. (b) DOFLC. (c) NAC. (d) Stator current THD comparison of three controllers. (Divisions: P_s – 500 W/div, Q_s – 500 var/div, ias – 6 A/div, iar – 2 A/div, time – 20 ms/div).

impacts of the voltage dip in stator current. It is significant that the use of VC results in large distortion of stator current when voltage dip is applied. There is around 2% increase of the THD by using DOFLC when voltage dips. With NAC, the voltage dip causes the smallest distortion of stator current when comparing to the VC and DOFLC. The comparison result verifies that the NAC improves the LVRT capability with uncertainty.

In Fig. 19, the amplitude of calculated rotor voltage after saturation is depicted. The outputs of those controllers in

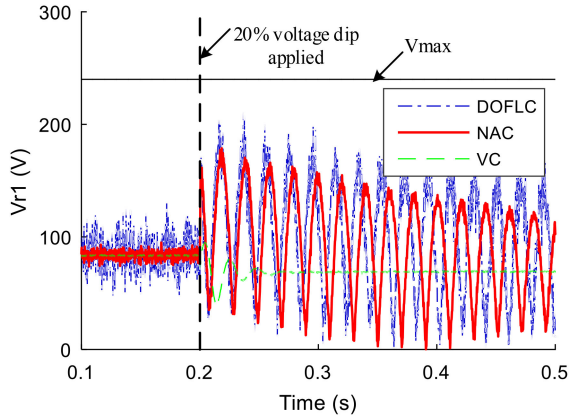

Fig. 19. Experiment result of the amplitude of calculated rotor voltage after saturation during a voltage dip.

comparative studies do not exceed the maximum amplitude of the RSC when a 20% voltage dip is applied. The DOFLC and the NAC generate a higher oscillated amplitude of the rotor voltage than the VC in order to compensate the disturbance caused by the voltage dip. With fast time-varying disturbance, the DOFLC cannot accurately estimate the actual disturbance, which results in larger rotor voltage and worse transient performance of the current dynamic than the NAC, as shown in Fig. 18(d).

V. Conclusion

A perturbation estimation based NAC has been proposed for decoupled control of the active/reactive power of the DFIG. The simulation and experiment tests have suggested that the proposed NAC provides fast dynamic response, strong robustness against parameter uncertainties, and improved LVRT capacities even with uncertainties. The perturbation observer is featured of estimating fast time-varying perturbations. Thus, the proposed NAC is capable of maintaining good dynamic performance when there are fast variations or mismatched values of system parameters during the transient processes of power tracking control or voltage dip responses. Moreover, the proposed NAC does not require full-state feedback and the detailed system model information, which implies that it has a simpler control structure than other nonlinear controllers. The measurement noises of the stator currents and voltages do not affect the performance of the proposed NAC.

Appendix A
Disturbance Observer Based FLC [28]

The DOFLC proposed in [28] is recalled here. A generic parameter P is defined as $P \in \{R_r, R_s, L_m, L_s, L_r, \sigma\}$ that includes all possible parameters of DFIG. The actual value of P can be presented by its nominal value plus uncertainty as $P = P_0 + \Delta P$. Then, the rotor current dynamics described in (10) can be rewritten as

$$\begin{cases} \dot{i}_{dr} = f_{d0} + g_{d0} v_{dr} + \Delta_d \\ \dot{i}_{qr} = f_{q0} + g_{q0} v_{qr} + \Delta_q \end{cases} \tag{A1}$$

where f_{d0}, f_{q0}, g_{d0}, and g_{q0} are the values of f_d, f_q, g_d, and g_q with nominal system parameters. $\Delta_{d,q}$ is defined to include all uncertainties, namely $\Delta_{d,q} = \Delta_{d,q}(\Delta P, i_{dr}, i_{qr}, i_{ds}, i_{qs}, v_{dr}, v_{qr}, v_{ds}, v_{qs})$.

A reduced-order observer is designed to estimate the disturbance terms Δ_d and Δ_q, the estimated terms are denoted as $\hat{\Delta}_d$ and $\hat{\Delta}_q$. The final DOFLC strategy for rotor current control can be expressed as

$$\begin{cases} v_{dr}^* = \frac{1}{g_{d0}} \left[i_{dr}^* - k_d \left(i_{dr} - i_{dr}^* \right) - f_{d0} - \hat{\Delta}_d \right] \\ v_{qr}^* = \frac{1}{g_{q0}} \left[i_{qr}^* - k_q \left(i_{qr} - i_{qr}^* \right) - f_{q0} - \hat{\Delta}_q \right]. \end{cases} \tag{A2}$$

In simulation studies of this paper, the observer gains of DOFLC is chosen to be $G_p = 2000$.

Appendix B
Stability Analysis of Closed-Loop System

The stability of the closed-loop system including controller/observer is investigated in this appendix, based on the approach in [39] and [48]. For the convenient of stability analysis, observers (20)–(21) have been represented in a compact form as

$$\begin{cases} \dot{\hat{x}}_{i1} = \hat{x}_{i2} + h_{i1}(x_{i1} - \hat{x}_{i1}) + b_{i0} u_i \\ \dot{\hat{x}}_{i2} = h_{i2}(x_{i1} - \hat{x}_{i1}) \end{cases} \tag{B1}$$

where $\tilde{x}_{ij} = x_{ij} - \hat{x}_{ij}$ refers to the estimation error of x_{ij}, $i = d, q$, $j = 1, 2$. By choosing

$$h_{i1} = \frac{\alpha_{i1}}{\varepsilon_i} \quad h_{i2} = \frac{\alpha_{i2}}{\varepsilon_i^2} \tag{B2}$$

and defining the scaled estimation errors

$$\eta_{i1} = \frac{\tilde{x}_{i1}}{\varepsilon_i} \quad \eta_{i2} = \tilde{x}_{i2} \tag{B3}$$

the observer error equation can be represented as

$$\varepsilon_i \dot{\eta}_{po_i} = A_{po_i} \eta_{po_i} + \varepsilon_i B_{po_i} \dot{\psi}_i \tag{B4}$$

where $\eta_{po_i} = [\eta_{i1} \eta_{i2}]^T$

$$A_{po_i} = \begin{bmatrix} -\alpha_{i1} & 1 \\ -\alpha_{i2} & 0 \end{bmatrix} \quad B_{po_i} = \begin{bmatrix} 0 \\ 1 \end{bmatrix}. \tag{B5}$$

The positive constants α_{i1} and α_{i2} are chosen such that A_{po_i} is a Hurwitzian matrix, and ε_i, $0 < \varepsilon_i \ll 1$, is a small positive parameter to be specified. This equation shows clearly that reducing ε_i diminishes the effect of $\dot{\psi}_i$. It also shows that, for ε_i small enough, the dynamics of the estimation error will be much faster than that of x_i.

Substituting control (22) into system (17), we have

$$\begin{cases} \dot{i}_{dr} = \dot{i}_{dr}^* - k_d(i_{dr} - i_{dr}^*) + \tilde{\Psi}_d \\ \dot{i}_{qr} = \dot{i}_{qr}^* - k_q(i_{qr} - i_{qr}^*) + \tilde{\Psi}_q \end{cases}$$

and defining tracking errors as $e_d = i_{dr} - i_{dr}^*$ and $e_q = i_{qr} - i_{qr}^*$, thus the dynamic of tracking errors is

$$\begin{cases} \dot{e}_d = -k_d e_d + \eta_{d2} \\ \dot{e}_q = -k_q e_q + \eta_{q2} \end{cases}$$

then

$$\dot{e}_i = A_{i0} e_i + B_{i0} \eta_{i2}$$

where $i = d, q$, $A_{i0} = [-k_i]$, and $B_{i0} = [1]$.

The closed-loop system including the tracking error system, controller, and observer can be represented as

$$e_i = A_{io} e_i - B_i \eta_{i2} \tag{B6}$$

$$\dot{\eta}_{po_i} = \frac{1}{\varepsilon_i} A_{po_i} \eta_{po_i} + B_{po_i} \dot{\psi}_i \tag{B7}$$

Assumption B: The perturbation Ψ_i and its derivative $\dot{\Psi}_i$ are Lipschitz in their arguments and bounded over the domain of interest. In addition, $\Psi(0) = 0$ and $\dot{\Psi}(0) = 0$.

Let us consider $V_i(e, \eta) = V_{i0}(e_i) + W_i(\eta_i)$ as a Lyapunov function candidate for subsystem (B6) and (B7), where

$$V_{i0}(e_i) = e_i^T P_{i1} e_i$$

over a ball $B(0, o_i) \subset R^3$, for some $o_i > 0$, and P_{i1} is the positive definite solution of the Lyapunov equation $P_{i1} A_{i0} + A_{i0}^T P_{i1} = -I_{i1}$, and

$$W_i(\eta_i) = \eta_{po_i}^T P_{i2} \eta_{po_i}$$

where P_{i2} is the positive definite solution of the Lyapunov equation $P_{i2} A_{po_i} + A_{po_i}^T P_{i2} = -I_{i2}$.

Choose $\xi_i < o_i$; then, given Assumption B, we have $\forall (e_i, \eta_{po_i}) \in B(0, \xi_i) \times \{\|\eta_{po_i}\| \le \xi_i\} = \Lambda_i$

$$|\dot{\Psi}_i(e_i, \eta_{po_i})| \le \gamma_{i2} \tag{B8}$$

where γ_{i2} is an upper bound of $\dot{\Psi}$. It can be shown that $\forall (e_i, \eta_{po_i}) \in \Lambda_i$, then, we have

$$\begin{aligned} \dot{V}_i &= \frac{\partial V_{i0}}{\partial x_i}(A_{i0} x + B_i \eta_{i2}) + \frac{\partial W_i}{\partial \eta_i} \left(\frac{1}{\varepsilon_i} A_{po_i} \eta_{po_i} + B_{po_i} \dot{\psi}_i \right) \\ &= -\|e_i\|^2 + 2 e_i^T P_{i1} B_i \eta_{i2} - \frac{1}{\varepsilon_i} \|\eta_{po_i}\|^2 + 2 \eta_{po_i}^T P_{i2} B_{po_i} \dot{\Psi} \\ &\le -\|e_i\|^2 - \frac{1}{\varepsilon_i} \|\eta_{po_i}\|^2 + 2 \|P_{i1}\| \|e_i\| \|\eta_{po_i}\| \\ &\quad + 2\gamma_{i2} \|P_{i2}\| \|\eta_{po_i}\| \\ &\le -\|e_i\| (\|e_i\| - 2 \|P_{i1}\| \|\eta_{po_i}\|) \\ &\quad - \|\eta_{po_i}\| \left(\frac{1}{\varepsilon_i} \|\eta_{po_i}\| - 2\gamma_{i2} \|P_{i2}\| \right). \end{aligned} \tag{B9}$$

Defining $\xi_{i2} = 2\varepsilon_i \gamma_2 \|P_{i2}\|$ and $\xi_{i1} = 2\varepsilon_i \|P_{i1}\| \xi_{i2} = 4\varepsilon_i \gamma_{i2} \|P_{i1}\| \|P_{i2}\|$; now for any given $\xi_i \le o_i$, we can choose

$$\varepsilon_i^* = \min \left\{ \frac{\xi_i}{8\gamma_{i2} \|P_{i0}\| \|P_{i1}\|}, \frac{\xi_i}{4\gamma_{i2} \|P_{i1}\|} \right\}.$$

Then $\forall \varepsilon_i, 0 < \varepsilon_i < \varepsilon_i^*$, we have $\|e_i\| \le \frac{\xi_i}{2}$, $\|\eta_{po_i}\| \le \frac{\xi_i}{2}$, $\|e_i\| \ge \xi_{i1}$, and $\|\eta_{po_i}\| \ge \xi_{i2}$, such that

$$\dot{V}_i \le -\|e_i\| (\|e_i\| - \xi_{i1}) - \|\eta_{po_i}\| (\|\eta_{po_i}\| - \xi_{i2}) \le 0.$$

Thus, there exists $T_i(\xi_i)$ and $T_1 > 0$, it can be shown that

$$\|e_i(t)\| + \|\eta_{po_i}\| \le \xi_i \; \forall t \ge T.$$

Note 1: Verification of Assumption B. Based on (11) and (16), as all physical variables are continuous and bounded, both perturbation terms (Ψ_d, Ψ_q) and their derivatives are bounded. Thus, Assumption B is satisfied.

Note 2: After the linearization of system (17), the zero dynamics of the remained nonlinearized system (1) are stable [28].

REFERENCES

[1] J. M. Carrasco *et al.*, "Power-electronic systems for the grid integration of renewable energy sources: A survey," *IEEE Trans. Ind. Electron.*, vol. 53, no. 4, pp. 1002–1016, Jun. 2006.

[2] B. Shen, B. Mwinyiwiwa, Y. Zhang, and B. T. Ooi, "Sensorless maximum power point tracking of wind by DFIG using rotor position phase lock loop (PLL)," *IEEE Trans. Power Electron.*, vol. 24, no. 4, pp. 942–951, Apr. 2009.

[3] G. D. Marques and M. F. Iacchetti, "Stator frequency regulation in a field-oriented controlled DFIG connected to a dc link," *IEEE Trans. Ind. Electron.*, vol. 61, no. 11, pp. 5930–5939, Nov. 2014.

[4] G. Tapia, A. Tapia, and J. Ostolaza, "Proportional-integral regulator-based approach to wind farm reactive power management for secondary voltage control," *IEEE Trans. Energy Convers.*, vol. 22, no. 2, pp. 488–498, Jun. 2007.

[5] J. Kim, J. K. Seok, E. Muljadi, and Y. C. Kang, "Adaptive Q–V scheme for the voltage control of a DFIG-based wind power plant," *IEEE Trans. Power Electron.*, vol. 31, no. 5, pp. 3586–3599, May 2016.

[6] R. Pena, J. Clare, and G. Asher, "Doubly fed induction generator using back-to-back PWM converters and its application to variable-speed wind-energy generation," *IEE Proc. Elect. Power Appl.*, vol. 143, no. 3, pp. 231–241, May 1996.

[7] M. Yamamoto and O. Motoyoshi, "Active and reactive power control for doubly-fed wound rotor induction generator," *IEEE Trans. Power Electron.*, vol. 6, no. 4, pp. 624–629, Oct. 1991.

[8] A. Petersson, L. Harnefors, and T. Thiringer, "Evaluation of current control methods for wind turbines using doubly-fed induction machines," *IEEE Trans. Power Electron.*, vol. 20, no. 1, pp. 227–235, Jan. 2005.

[9] H. Akagi and H. Sato, "Control and performance of a doubly-fed induction machine intended for a flywheel energy storage system," *IEEE Trans. Power Electron.*, vol. 17, no. 1, pp. 109–116, Jan. 2002.

[10] S. Chondrogiannis and M. Barnes, "Stability of doubly-fed induction generator under stator voltage orientated vector control," *IET Renewable Power Gener.*, vol. 2, no. 3, pp. 170–180, Sep. 2008.

[11] E. Tremblay, S. Atayde, and A. Chandra, "Comparative study of control strategies for the doubly fed induction generator in wind energy conversion systems: A DSP-based implementation approach," *IEEE Trans. Sustain. Energy*, vol. 2, no. 3, pp. 288–299, Jul. 2011.

[12] J. F. Hu, J. Zhu, Y. Zhang, G. Platt, Q. Ma, and D. G. Dorrell, "Predictive direct virtual torque and power control of doubly fed induction generators for fast and smooth grid synchronization and flexible power regulation," *IEEE Trans. Power Electron.*, vol. 28, no. 7, pp. 3182–3194, Jul. 2013.

[13] D. Zhi, L. Xu, and B. W. Williams, "Model-based predictive direct power control of doubly fed induction generators," *IEEE Trans. Power Electron.*, vol. 25, no. 2, pp. 341–351, Feb. 2010.

[14] J. Hu, H. Nian, B. Hu, Y. He, and Z. Zhu, "Direct active and reactive power regulation of DFIG using sliding-mode control approach," *IEEE Trans. Energy Convers.*, vol. 25, no. 4, pp. 1028–1039, Dec. 2010.

[15] A. Feijo, J. Cidrs, and C. Carrillo, "A third order model for the doubly-fed induction machine," *Elect. Power Syst. Res.*, vol. 56, no. 2, pp. 121–127, 2000.

[16] Y. Lei, A. Mullane, G. Lightbody, and R. Yacamini, "Modeling of the wind turbine with a doubly fed induction generator for grid integration studies," *IEEE Trans. Energy Convers.*, vol. 21, no. 1, pp. 257–264, Mar. 2006.

[17] J. Ekanayake, L. Holdsworth, and N. Jenkins, "Comparison of 5th order and 3rd order machine models for doubly fed induction generator (DFIG) wind turbines," *Elect. Power Syst. Res.*, vol. 67, no. 3, pp. 207–215, 2003.

[18] S. Hu, X. Lin, Y. Kang, and X. Zou, "An improved low-voltage ride-through control strategy of doubly fed induction generator during grid faults," *IEEE Trans. Power Electron.*, vol. 26, no. 12, pp. 3653–3665, Dec. 2011.

[19] H. Chaal and M. Jovanovic, "Toward a generic torque and reactive power controller for doubly fed machines," *IEEE Trans. Power Electron.*, vol. 27, no. 1, pp. 113–121, Jan. 2012.

[20] H. Nian and Y. Song, "Direct power control of doubly fed induction generator under distorted grid voltage," *IEEE Trans. Power Electron.*, vol. 29, no. 2, pp. 894–905, Feb. 2014.

[21] L. Xu and P. Cartwright, "Direct active and reactive power control of DFIG for wind energy generation," *IEEE Trans. Energy Convers.*, vol. 21, no. 3, pp. 750–758, Sep. 2006.

[22] S. Mondal and D. Kastha, "Improved direct torque and reactive power control of a matrix-converter-fed grid-connected doubly fed induction generator," *IEEE Trans. Ind. Electron.*, vol. 62, no. 12, pp. 7590–7598, Dec. 2015.

[23] P. Xiong and D. Sun, "Backstepping-based DPC strategy of a wind turbine-driven DFIG under normal and harmonic grid voltage," *IEEE Trans. Power Electron.*, vol. 31, no. 6, pp. 4216–4225, Jun. 2016.

[24] G. Rigatos, P. Siano, N. Zervos, and C. Cecati, "Control and disturbances compensation for doubly fed induction generators using the derivative-free nonlinear Kalman filter," *IEEE Trans. Power Electron.*, vol. 30, no. 10, pp. 5532–5547, Oct. 2015.

[25] A. Balogun, O. Ojo, and F. Okafor, "Decoupled direct control of natural and power variables of doubly fed induction generator for extended wind speed range using feedback linearization," *IEEE J. Emerg. Sel. Topics Power Electron.*, vol. 1, no. 4, pp. 226–237, Dec. 2013.

[26] M. Mohseni, S. Islam, and M. Masoum, "Enhanced hysteresis-based current regulators in vector control of DFIG wind turbines," *IEEE Trans. Power Electron.*, vol. 26, no. 1, pp. 223–234, Jan. 2011.

[27] J. Mohammadi, S. V.-Z. Adeh, S. Afsharnia, and E. Daryabeigi, "A combined vector and direct power control for DFIG-based wind turbines," *IEEE Trans. Sustain. Energy*, vol. 5, no. 3, pp. 767–775, Jul. 2014.

[28] J. Mauricio, A. Leon, A. Gomez-Exposito, and J. Solsona, "An adaptive nonlinear controller for DFIM-based wind energy conversion systems," *IEEE Trans. Energy Convers.*, vol. 23, no. 4, pp. 1025–1035, Dec. 2008.

[29] G. Chen, L. Zhang, X. Cai, W. Zhang, and C. Yin, "Nonlinear control of the doubly fed induction generator by input-output linearizing strategy," in *Electronics and Signal Processing* (Lecture Notes in Electrical Engineering), vol. 97, W. Hu, Ed. Berlin, Germany: Springer, 2011, pp. 601–608.

[30] R. Zhu, Z. Chen, Y. Tang, F. Deng, and X. Wu, "Dual-loop control strategy for DFIG-based wind turbines under grid voltage disturbances," *IEEE Trans. Power Electron.*, vol. 31, no. 3, pp. 2239–2253, Mar. 2016.

[31] Q. Huang, X. Zou, D. Zhu, and Y. Kang, "Scaled current tracking control for doubly fed induction generator to ride-through serious grid faults," *IEEE Trans. Power Electron.*, vol. 31, no. 3, pp. 2150–2165, Mar. 2016.

[32] M. Mohseni and S. M. Islam, "Transient control of DFIG-based wind power plants in compliance with the Australian grid code," *IEEE Trans. Power Electron.*, vol. 27, no. 6, pp. 2813–2824, Jun. 2012.

[33] H. Geng, C. Liu, and G. Yang, "LVRT capability of DFIG-based WECS under asymmetrical grid fault condition," *IEEE Trans. Ind. Electron.*, vol. 60, no. 6, pp. 2495–2509, Jun. 2013.

[34] Z. Xie, X. Zhang, X. Zhang, S. Yang, and L. Wang, "Improved ride-through control of DFIG during grid voltage swell," *IEEE Trans. Ind. Electron.*, vol. 62, no. 6, pp. 3584–3594, Jun. 2015.

[35] W. Chen, D. Xu, N. Zhu, M. Chen, and F. Blaabjerg, "Control of doubly-fed induction generator to ride-through recurring grid faults," *IEEE Trans. Power Electron.*, vol. 31, no. 7, pp. 4831–4846, Jul. 2016.

[36] J. P. da Costa, H. Pinheiro, T. Degner, and G. Arnold, "Robust controller for DFIGs of grid-connected wind turbines," *IEEE Trans. Ind. Electron.*, vol. 58, no. 9, pp. 4023–4038, Sep. 2011.

[37] J.-J. E. Slotine and W. Li, *Applied Nonlinear Control*. Upper Saddle River, NJ, USA: Prentice-Hall, 1991.

[38] W. H. Chen, J. Yang, L. Guo, and S. Li, "Disturbance-observer-based control and related methods—An overview," *IEEE Trans. Ind. Electron.*, vol. 63, no. 2, pp. 1083–1095, Feb. 2016.

[39] L. Jiang, Q. Wu, and J. Wen, "Decentralized nonlinear adaptive control for multi-machine power systems via high-gain perturbation observer," *IEEE Trans. Circuits Syst. I*, vol. 51, no. 10, pp. 2052–2059, Oct. 2004.

[40] Y. Liu, Q. H. Wu, X. X. Zhou, and L. Jiang, "Perturbation observer based multiloop control for the DFIG-WT in multimachine power system," *IEEE Trans Power Syst.*, vol. 29, no. 6, pp. 2905–2915, Nov. 2014.

[41] R. Cardenas, R. Pena, S. Alepuz, and G. Asher, "Overview of control systems for the operation of DFIGs in wind energy applications," *IEEE Trans. Ind. Electron.*, vol. 60, no. 7, pp. 2776–2798, Jul. 2013.

[42] A. Tapia, G. Tapia, J. X. Ostolaza, and J. R. Saenz, "Modeling and control of a wind turbine driven doubly fed induction generator," *IEEE Trans. Energy Convers.*, vol. 18, no. 2, pp. 194–204, Jun. 2003.

[43] J. Slootweg, S. de Haan, H. Polinder, and W. Kling, "General model for representing variable speed wind turbines in power system dynamics simulations," *IEEE Trans. Power Syst.*, vol. 18, no. 1, pp. 144–151, Feb. 2003.
[44] S. Li, T. Haskew, K. Williams, and R. Swatloski, "Control of DFIG wind turbine with direct-current vector control configuration," *IEEE Trans. Sustain. Energy*, vol. 3, no. 1, pp. 1–11, Jan. 2012.
[45] W.-H. Chen, D. J. Ballance, P. J. Gawthrop, and J. O'Reilly, "A nonlinear disturbance observer for robotic manipulators," *IEEE Trans. Ind. Electron.*, vol. 47, no. 4, pp. 932–938, Aug. 2000.
[46] G. Abad, J. López, M. Rodríguez, L. Marroyo, and G. Iwanski, *Doubly Fed Induction Machine: Modeling and Control for Wind Energy Generation Applications*. Hoboken, NJ, USA: Wiley, 2011.
[47] D. Xiang, L. Ran, P. J. Tavner, and S. Yang, "Control of a doubly fed induction generator in a wind turbine during grid fault ride-through," *IEEE Trans. Energy Convers.*, vol. 21, no. 3, pp. 652–662, Sep. 2006.
[48] H. K. Khalil, *Nonlinear Systems*. Upper Saddle River, NJ, USA: Prentice-Hall, 2002.

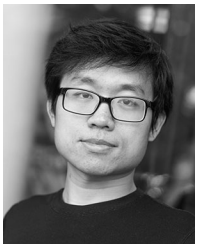

Kai Shi received the B.Eng. and Ph.D. degrees in electrical engineering and electronics from the University of Liverpool, Liverpool, U.K., in 2013 and 2017, respectively.

He is currently a Research Fellow with the Warwick Manufacturing Group, University of Warwick, Coventry, U.K. His research interests include battery management system, renewable energy, control of power electronics converters, and electric vehicles.

Xin Yin received the B.Eng. degree in electronic engineering from The University of Sheffield, Sheffield, U.K., in 2008, the M.Sc. degree in telecommunication from University College London, London, U.K., in 2009, and the Ph.D. degree in electrical and electronic engineering from The University of Manchester, Manchester, U.K., in 2016.

He is currently a Postdoctoral Research Associate of electrical engineering with the University of Liverpool, Liverpool, U.K. His current research interests include control of microgrid with renewable energy and demand side response.

Lin Jiang (M'00) received the B.S. and M.S. degrees in electrical engineering from Huazhong University of Science and Technology, Wuhan, China, in 1992 and 1996, respectively, and the Ph.D. degree in electrical engineering from the University of Liverpool, Liverpool, U.K., in 2001.

He was a Postdoctoral Research Assistant with the University of Liverpool from 2001 to 2003, and a Postdoctoral Research Associate with the Department of Automatic Control and Systems Engineering, The University of Sheffield from 2003 to 2005. He was a Senior Lecturer with the University of Glamorgam from 2005 to 2007 and moved to the University of Liverpool in 2007. He is currently a Reader with the University of Liverpool. His current research interests include control and analysis of power systems, smart grids, and renewable energy.

Yang Liu received the B.E. and Ph.D. degrees in electrical engineering from South China University of Technology (SCUT), Guangzhou, China, in 2012 and 2017, respectively.

He is currently a Lecturer with the SCUT. He has authored or coauthored more than 20 peer-reviewed SCI journal papers. His research interests include the areas of power system stability analysis and control, control of wind power generation systems, and nonlinear control theory.

Yihua Hu (M'13–SM'15) received the B.S. degree in electrical engineering and the Ph.D. degree in power electronics and drives from China University of Mining and Technology, Xuzhou, China, in 2003 and 2011, respectively.

Between 2011 and 2013, he was with the College of Electrical Engineering, Zhejiang University, as a Postdoctoral Fellow. Between 2013 and 2015, he was a Research Associate with the Power Electronics And Motor Drive Group, University of Strathclyde. He is currently a Lecturer with the Department of Electrical Engineering and Electronics, University of Liverpool, Liverpool, U.K. He has authored or coauthored 75 papers in IEEE Transactions journals. His research interests include renewable generation, power electronics converters and control, electric vehicles, more electric ship/aircraft, smart energy systems, and nondestructive test technology.

He is the Associate Editor for the *IET Renewable Power Generation, IET Intelligent Transport Systems*, and *Power Electronics and Drives*.

Huiqing Wen (M'13–SM'18) received the B.S. and M.S. degrees in electrical engineering from Zhejiang University, Hangzhou, China, in 2002 and 2006, respectively, and the Ph.D. degree in electrical engineering from the Chinese Academy of Sciences, Beijing, China, in 2009.

From 2009 to 2010, he was an Electrical Engineer with the GE (China) Research and Development Center Company, Ltd., Shanghai, China. From 2010 to 2011, he was an Engineer with the China Coal Research Institute, Beijing, China. From 2011 to 2012, he was a Postdoctoral Fellow with Masdar Institute of Science and Technology, Abu Dhabi, United Arab Emirates. In 2013, he joined the Electrical and Electronic Engineering Department, Xi'an Jiaotong-Liverpool University (XJTLU), Suzhou, China. He is currently a Senior Associate Professor with the XJTLU. He has authored or coauthored more than 100 peer-reviewed technical papers in leading journals/conferences and holds more than 20 issued/pending patents. His research interests include renewable energy, electric vehicles, power electronics, microgrids, and power semiconductor devices.

He is the Associate Editor for the IEEE ACCESS, *International Journal of Photoenergy*, and *Journal of Power Electronics*.